ACS APPLIED MATERIALS & INTERFACES

www.acsami.org

Research Article

Mechanism of Nitrogen-Doped Ti_3C_2 Quantum Dots for Free-Radical Scavenging and the Ultrasensitive H_2O_2 Detection Performance

Lifeng Wang,[⊥] Ningning Zhang,[⊥] Yan Li,* Wenhui Kong, Jingyun Gou, Yujuan Zhang, Lu-Ning Wang, Guanghua Yu, Ping Zhang, Huhu Cheng, and Liangti Qu*

Cite This: *ACS Appl. Mater. Interfaces* 2021, 13, 42442−42450

Read Online

ACCESS | Metrics & More | Article Recommendations | Supporting Information

ABSTRACT: MXene quantum dots feature favorable biological compatibility and superior optical properties, offering great potential for biomedical applications such as reactive oxygen species (ROS) scavenging and fluorescence sensing. However, the ROS scavenging mechanism is still unclear and the MXene-based materials for ROS sensing are still scarce. Here, we report a nitrogen-doped titanium carbide quantum dot (N-Ti_3C_2 QD) antioxidant with effective ROS scavenging ability. The doped nitrogen atoms promote the electrochemical interaction between N-Ti_3C_2 QDs and free radicals and thus enhance their antioxidant performance. Density functional theory (DFT) simulations reveal the hydroxyl radical quenching process and confirm that the doped N element promotes the free-radical absorption ability, especially for −F and −O functional groups in N-Ti_3C_2 QDs. Furthermore, N-Ti_3C_2 QDs show rapid, accurate, and remarkable sensitivity to hydrogen peroxide in the range of 5 nM−5.5 μM with a limit of detection of 1.2 nM within 15 s, which is the lowest detection limit of the existing fluorescent probes up to now. Our results provide a new category of antioxidant materials, a real-time hydrogen peroxide sensing probe, promoting the research and development of MXene in bioscience and biotechnology.

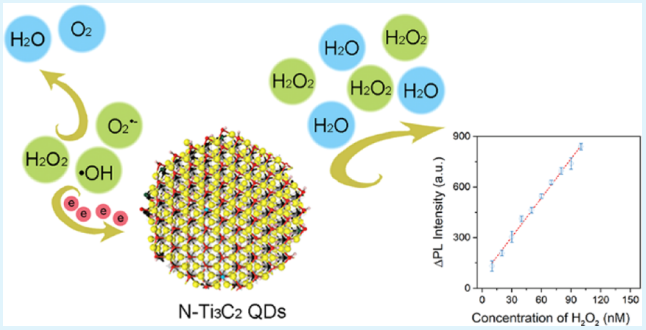

KEYWORDS: *nitrogen-doped titanium carbide quantum dots, antioxidants, functional groups, fluorescence biosensor, H_2O_2*

INTRODUCTION

Reactive oxygen species (ROS), including singlet oxygen, superoxide anion, hydrogen peroxide (H_2O_2), and hydroxyl radicals, play an important role in cellular life cycles such as proliferation and homeostasis.[1,2] However, high ROS levels are detrimental to cellular components cell membranes, protein structures, and DNA, which can damage cellular functions.[3−5] It is urgent to develop high-efficiency and low-toxicity antioxidants materials for biomedical research and clinical applications. Furthermore, disorder or accumulation of ROS could lead to several severe diseases such as cancer, Alzheimer's, central nervous system diseases, kidney disorders, and aging.[6,7] Consequently, accurate and highly sensitive detection of the related ROS concentration (mainly H_2O_2) is critical for earlier catching and treating these diseases.

With the fast development in nanomedicine, a variety of nanomaterials with ROS scavenging activities have been reported such as metal nanoclusters,[8] metal oxide nanoparticles,[9,10] 2D materials (including graphene,[11] black phosphorus,[12] transition-metal dichalcogenides,[13] and MXene[14]), and their derivatives.[15−17] Among them, zero-dimensional QDs derived from 2D MXene have recently attracted tremendous attention in biomedical fields owing to their favorable biological compatibility and unique physicochemical properties.[18,19] The strong quantum confinement, abundant active edge sites, and a high surface-to-volume ratio promote such QD materials' efficient activities and they can serve as free-radical scavengers. Ren et al. reported that niobium carbide (Nb_2C) MXene could effectively protect the cells and mice from ionizing radiation-induced ROS damage.[14] Our group confirmed that Cl- and N-codoped Ti_3C_2 QDs exhibit outstanding hydroxyl radical scavenging performance.[20] However, the free-radical scavenging mechanism of MXene-based materials and the contribution of the functional groups and dopants are still confusing.

Apart from scavenging free radicals to suppress oxidative stress, these nanomaterials have also been widely used as ROS probes to monitor human health or diagnose ROS-related diseases.[21] Hydrogen peroxide, as the most important marker for ROS, not only participates in several cellular processes but also connects to aging and some serious diseases.[22] Until now,

Received: June 16, 2021
Accepted: August 24, 2021
Published: September 2, 2021

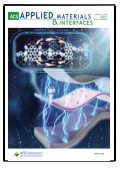

https://doi.org/10.1021/acsami.1c11242
ACS Appl. Mater. Interfaces 2021, 13, 42442−42450

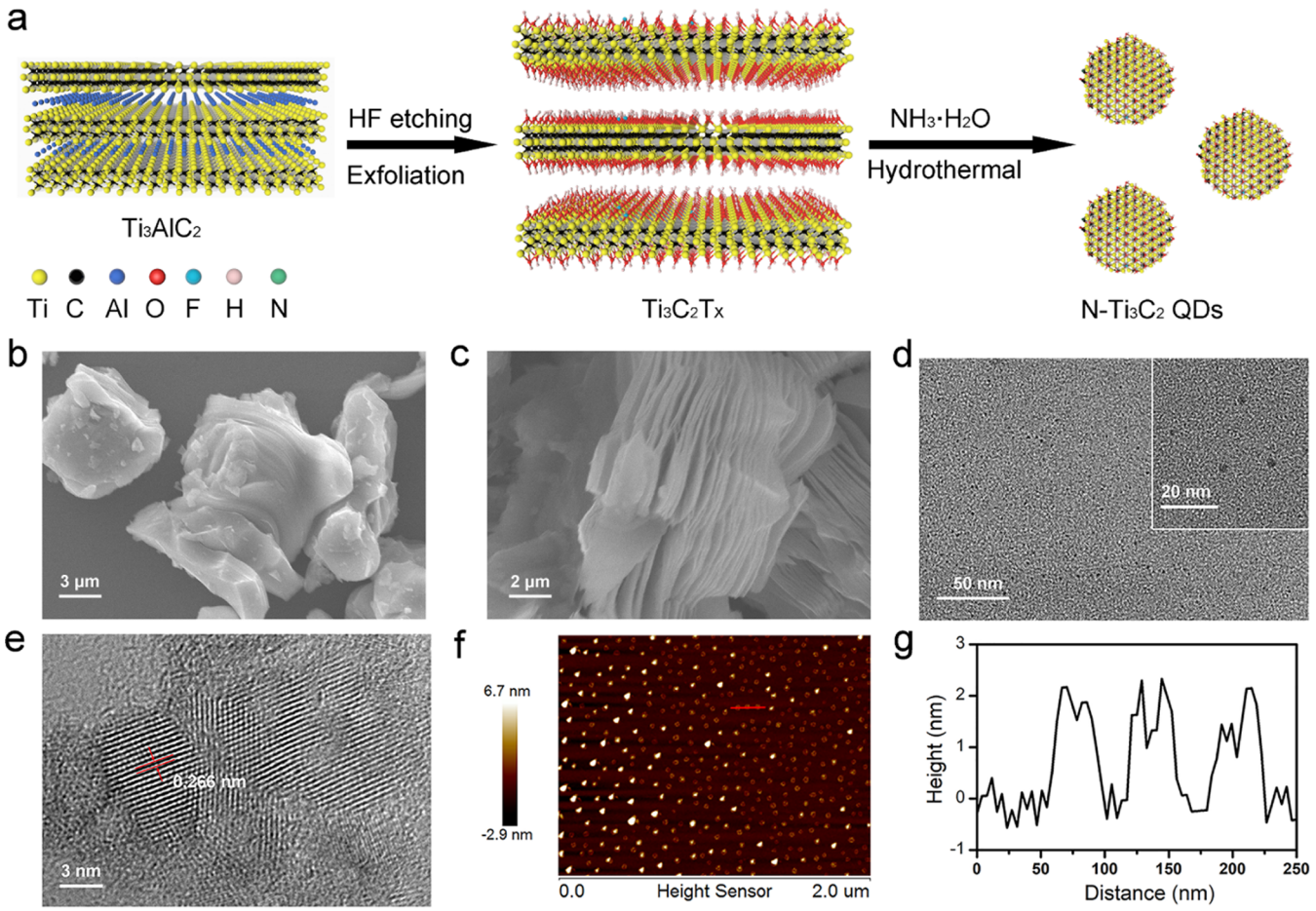

Figure 1. Schematic of synthesis and the morphology N-Ti_3C_2 QDs. (a) Schematic illustration of the preparation of N-Ti_3C_2 QDs. Typical SEM images of (b) Ti_3AlC_2 and (c) HF-etched $Ti_3C_2T_x$. TEM (d) and HRTEM (e) images of N-Ti_3C_2 QDs (the inset shows the high-resolution TEM image of N-Ti_3C_2 QDs). The AFM image (f) and the height profile (g) of N-Ti_3C_2 QDs.

there have been methods for detecting H_2O_2, including chemiluminescence, electrochemistry, chromatography, etc.,[23−27] but these methods either need a complicated operation and high cost of instrumental analysis or have low sensitivity and difficulty in on-site monitoring. Therefore, fluorescence methods have gathered significant interest due to simple instruments and easy operation.[28] Nonetheless, the previously reported fluorescent probes exhibit unsatisfactory sensitivity. The high activity of N-Ti_3C_2 QDs to H_2O_2 and their outstanding biological compatibility as well as the intrinsic fluorescence properties show their promising potential in the H_2O_2-sensing field.

In this study, we reported an efficient antioxidant material based on MXene. The N-Ti_3C_2 QDs were synthesized by a hydrothermal method, using ammonium hydroxide as a nitrogen source. The trace level doping of nitrogen atoms could modulate the intrinsic structure of Ti_3C_2 QDs and bring about excellent ROS scavenging performance. The scavenging efficiency of N-Ti_3C_2 QDs is superior to Ti_3C_2 QDs, graphene oxide (GO), and graphene quantum dots (GQDs). In addition, with the help of readily oxidizable Ti^{2+} and small quantities of nitrogen doping, N-Ti_3C_2 QDs demonstrated superior H_2O_2 detection sensitivity with a detection limit of 1.2 nM, which is the lowest detection limit of the existing fluorescent probes for H_2O_2. Our results open a novel perspective for the application of MXene QDs in biomedical and biosensor fields.

RESULTS AND DISCUSSION

Synthesis and Characterization of N-Ti_3C_2 QDs. The synthesis procedure of N-Ti_3C_2 QDs is shown in Figure 1a. Briefly, the aluminum layers of the Ti_3AlC_2 ceramic powder is etched by HF acid and resulting multilayer $Ti_3C_2T_x$ (T_x = OH, O, or F). After selective etching, the as-prepared $Ti_3C_2T_x$ exhibited a loosely layered structure with an average edge length of several micrometers, as shown in the SEM image (Figure 1c). The strongest diffraction peak around 9.62° of Ti_3AlC_2 shifts toward lower angles after etching, implying that the *c*-axis lattice constantly increases and layer spacing is enlarged (Figure S1).[29,30] Furthermore, the broadened (002) characteristic peaks in the $Ti_3C_2T_x$ sample indicate the decrease in the crystallinity after the aluminum atoms were etched.[31] Finally, N-Ti_3C_2 QDs could be obtained via hydrothermally cutting $Ti_3C_2T_x$ sheets using ammonium hydroxide as a nitrogen source. TEM images (Figure 1d) show that N-Ti_3C_2 QDs are uniformly dispersed. The high-resolution TEM image (Figure 1e) exhibits the lattice fringes with an inner-plane spacing at 0.266 nm, corresponding to the (0110) crystal plane of $Ti_3C_2T_x$ and confirms that the N-Ti_3C_2 QDs well preserved the crystal structure of pristine $Ti_3C_2T_x$ nanosheets.[18] The AFM image and the height profile of N-Ti_3C_2 QDs (Figure 1f,g) show that the N-Ti_3C_2 QDs have a similar thickness of about 2 nm, which corresponds to two layers of MXene.[19]

https://doi.org/10.1021/acsami.1c11242
ACS Appl. Mater. Interfaces 2021, 13, 42442−42450

The chemical structure, composition, and functional groups of N-Ti_3C_2 QDs are explored by FT-IR and XPS spectra. As shown in Figure 2a, in addition to the similar stretching

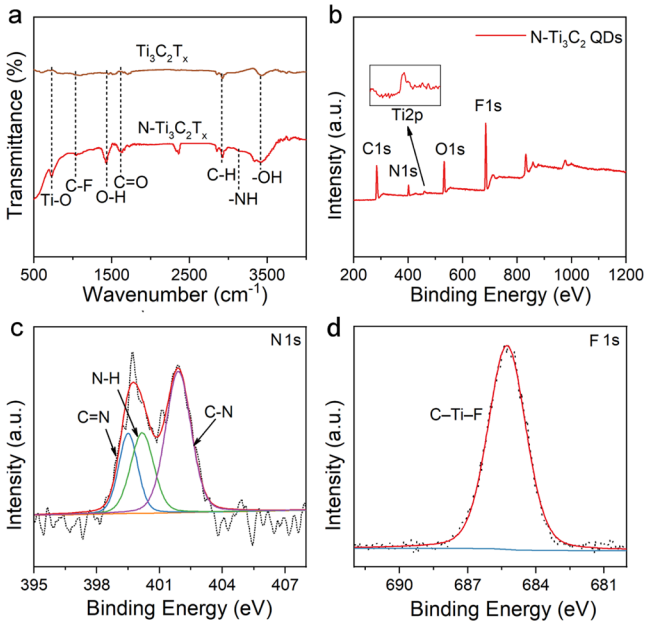

Figure 2. Chemical structure of N-Ti_3C_2 QDs. (a) FT-IR spectra of $Ti_3C_2T_x$ and N-Ti_3C_2 QDs. (b) XPS survey of N-Ti_3C_2 QDs. (c) N 1s spectrum of N-Ti_3C_2 QDs. (d) F 1s spectrum of N-Ti_3C_2 QDs.

vibrations of $Ti_3C_2T_x$ nanosheets and N-Ti_3C_2 QDs, including Ti−O at 665 cm^{-1}, C−F at 1100 cm^{-1}, C═O at 1650 cm^{-1}, and −OH around 3430 cm^{-1}, N-Ti_3C_2 QDs shows the −NH stretching vibration at 3120 cm^{-1}.[32] The appearance of a new peak indicates that nitrogen is bonded to Ti_3C_2 QDs successfully. This result is also confirmed by the XPS spectra, which show that the C 1s peak at 284.0 eV, the O 1s peak at 530.0 eV, the Ti 2p peak at 460.0 eV, the F 1s peak at 685.0 eV, and the N 1s peak at 400.0 eV are present, as shown in Figure 2b, demonstrating the successful doping of the nitrogen element, which is absent in the Ti_3C_2 QD sample (Figures S3 and S4). In addition, N atoms mainly bond with C atoms (Figure 2c) and F atoms attach to the Ti layer and serve as functional groups (Figure 2d).

Antioxidant Performance of N-Ti_3C_2 QDs. Next, we evaluate the antioxidant performance of N-Ti_3C_2 QDs. The way of antioxidants to scavenge free radicals could be summarized as hydrogen donation, adduct formation, and charge transfer.[15] Herein, DPPH• scavenging assay was conducted to evaluate the hydrogen donation ability of N-Ti_3C_2 QDs. In the DPPH• scavenging process, DPPH• captures the hydrogen atoms from N-Ti_3C_2 QDs and is converted into a stable DPPH-H complex accompanied by the color change from deep violet to light yellow. Figure S5 reveals that N-Ti_3C_2 QDs exhibit poor DPPH• scavenging ability even with N doping, indicating that N-Ti_3C_2 QDs possess weaker hydrogen donation ability compared to the previously reported GQDs.[33] Subsequently, the adduct formation and charge-transfer free-radical scavenging models were quantitatively determined by •OH scavenging assay. Hydroxyl radicals, the most reactive chemical species, could be rapidly captured by terephthalic acid and form fluorescent product 2-hydroxyterephthalic acid, which could be monitored by fluorescence measurements. As shown in Figure 3a, N-Ti_3C_2 QDs feature the highest •OH scavenging efficiency (93.2%), which is superior to Ti_3C_2 QDs (65.9%). GO and GQDs possess favorable antioxidant performance according to previous reports.[11,33] Under the same concentrations, the •OH scavenging ratios of GO and GQDs are 37.3 and 53.3%, respectively. The high •OH scavenging activity of N-Ti_3C_2

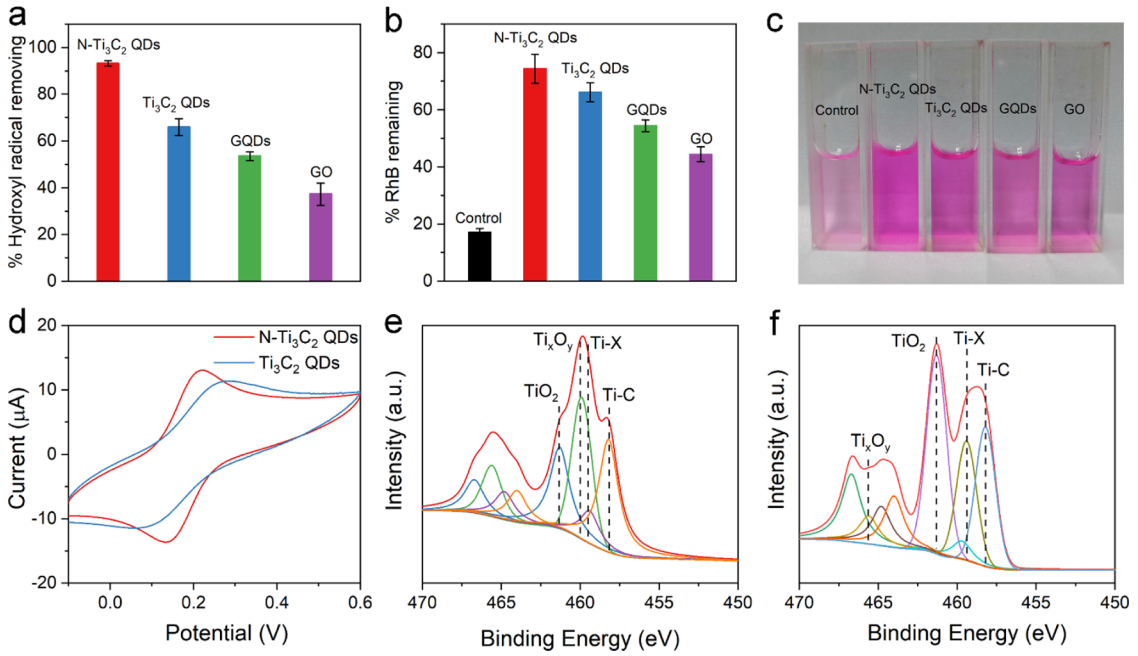

Figure 3. Antioxidant performance of N-Ti_3C_2 QDs. (a) •OH scavenging performance of N-Ti_3C_2 QDs, Ti_3C_2 QDs, GQDs, and GO. The ratio of remaining RhB (b) and the photos (c) after photocatalytic degradation with N-Ti_3C_2 QDs, Ti_3C_2 QDs, GQDs, and GO. (d) CV curves of N-Ti_3C_2 QD and Ti_3C_2 QD samples. High-resolution Ti 2p spectra of N-Ti_3C_2 QDs before (e) and after (f) reacting with •OH.

https://doi.org/10.1021/acsami.1c11242
ACS Appl. Mater. Interfaces 2021, 13, 42442−42450

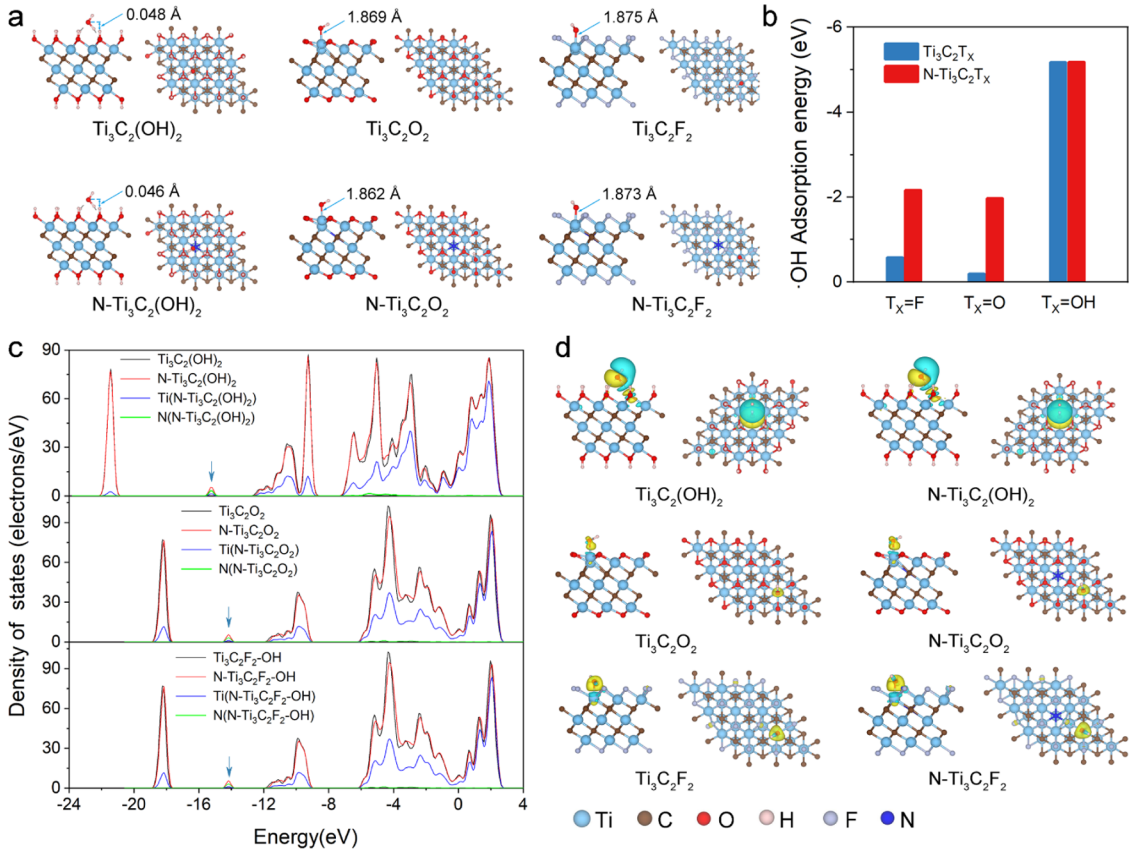

Figure 4. Interaction between •OH and $Ti_3C_2T_x$. The side view and the top view for the relaxed structures of •OH adsorbed on the $Ti_3C_2T_x$ and $N\text{-}Ti_3C_2T_x$ surfaces (a) and the corresponding absorption energy (b). (c) Density of states for $Ti_3C_2T_x$ and $N\text{-}Ti_3C_2T_x$. (d) Side view and the top view for charge density distribution of $Ti_3C_2T_x$-OH and $N\text{-}Ti_3C_2T_x$-OH. Charge accumulation (depletion) is represented in yellow (cyan).

QDs could be ascribed to their excellent •OH absorbability and high-efficiency charge-transfer ability.

Robust scavenging ability to multiple primary and secondary ROS is another standard for antioxidants.[34] Here, the antioxidative activities of $N\text{-}Ti_3C_2$ QDs against multiple ROS including $^1O_2$, •OH, $O_2^{\bullet-}$, and H_2O_2, are assessed by organic-dye-protecting experiments. To avoid the exogenous disturbance in the ROS generation process, the in situ-generated $^1O_2$, •OH, $O_2^{\bullet-}$, and H_2O_2 via a photochemical reaction by P25 TiO_2 are used for quantitatively assessing the scavenging performance of multiple radicals of $N\text{-}Ti_3C_2$ QDs.[35] ROS produced by UV (365 nm)-excited TiO_2 nanoparticles could be scavenged by $N\text{-}Ti_3C_2$ QDs and inhibits the rhodamine B molecule degradation. As shown in Figure 3b, $N\text{-}Ti_3C_2$ QDs own the highest dye protection efficiency (74.3%), which is better than Ti_3C_2 QDs (66.1%), GQDs (54.4%), and GO (44.4%), suggesting that the scavenging performances of $N\text{-}Ti_3C_2$ QDs for the full range of ROS are superior to previous graphene-based antioxidants. In addition, $N\text{-}Ti_3C_2$ QDs also show (Figure S7) excellent scavenging performance for $^1O_2$ and $O_2^{\bullet-}$, respectively.

The superior antioxidant performance of $N\text{-}Ti_3C_2$ QDs could be attributed to the doping of nitrogen atoms, which is analogous to the heteroatom-doped GQDs.[16] The doped nitrogen atoms promote the electron-transfer ability between $N\text{-}Ti_3C_2$ QDs and free radicals. Cyclic voltammetry (CV) measurements are adopted to verify this assumption.[36] As shown in Figure 3d, the redox peak of $N\text{-}Ti_3C_2$ QDs has higher redox current than Ti_3C_2 QDs. In addition, the CV curve of $N\text{-}Ti_3C_2$ QDs shows a narrower peak-to-peak potential separation (ΔE_P) of 78 mV, which testifies that the charge-transfer kinetics of the redox reaction of $K_3[Fe(CN)_6]$ and $K_4Fe(CN)_6$ at $N\text{-}Ti_3C_2$ QDs is easier than the Ti_3C_2 QD-modified electrode (184 mV).[37] This represents that $N\text{-}Ti_3C_2$ QDs have better electron-transfer capabilities because doping of nitrogen atoms introduces more defects and provides more active sites. As demonstrated in Figure 3e, partial N atoms replace C atoms and bond with Ti atoms (462.3 eV in the Ti 2p spectrum). The results (Figures 2c and 3e) indicate that N atoms replace C atoms between the Ti atom layer or/and connect to C atoms at the edge of the MXene structure. After reacting with •OH, XPS investigations are performed again to determine the change in $N\text{-}Ti_3C_2$ QDs. Figure S8 shows that the N atom ratio reduces to 2.52% but still exists between the Ti atom layer (Ti−X bond shown in Figure 3f) and on the edge of $N\text{-}Ti_3C_2$ QDs (C−N bond shown in Figure S8b). However, the XPS spectra of Ti 2p show that Ti^{4+} increases from 24.9 to 40.4% (Figure 3e,f) after the scavenging reaction, indicating that the ROS scavenging could be ascribed to the charge transfer from •OH, leading to the gradual oxidation of $N\text{-}Ti_3C_2$ QDs.

DFT Simulation. To evaluate the adsorption energies of •OH on the $Ti_3C_2T_x$ or $N\text{-}Ti_3C_2T_x$ (T_x = −OH, −O, or F, according to the FT-IR and XPS survey shown in Figure 2a,d) nanosheets, we define the adsorption energy (E_{ads}) as

$$E_{ads} = E_{total} - E_{surface} - E_{\bullet OH,isolated} \quad (1)$$

https://doi.org/10.1021/acsami.1c11242
ACS Appl. Mater. Interfaces 2021, 13, 42442−42450

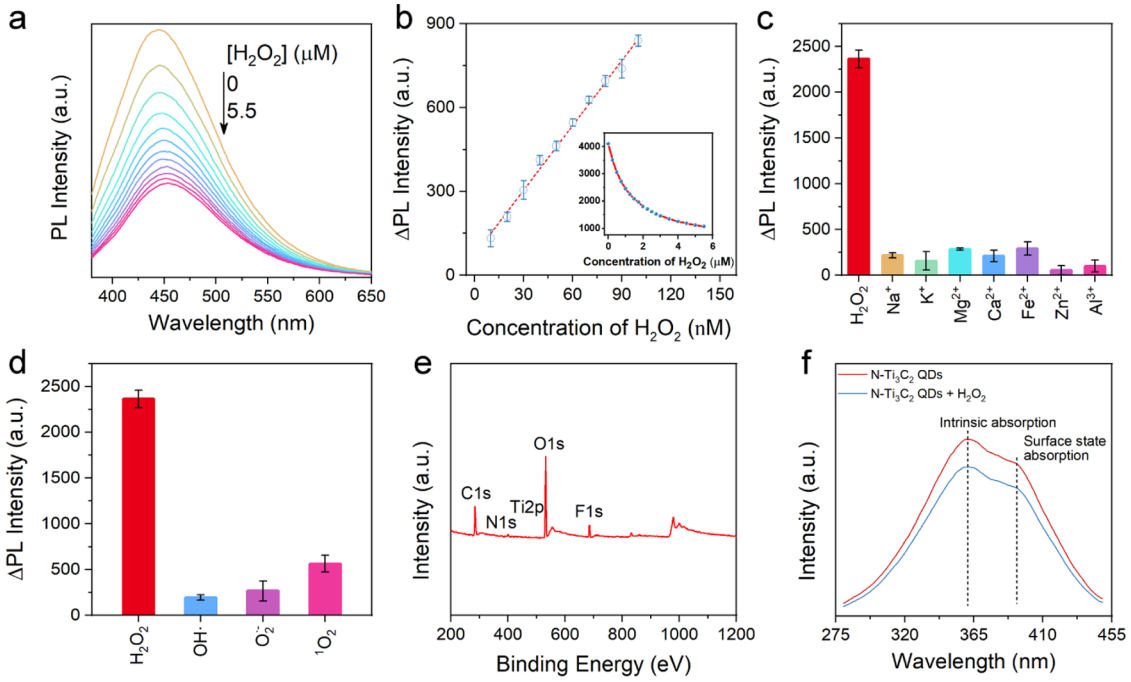

Figure 5. H_2O_2-sensing performance of N-Ti_3C_2 QDs. (a) PL intensity variation of N-Ti_3C_2 QDs with different concentrations of H_2O_2 (0−5.5 μM). (b) Linear relationship between N-Ti_3C_2 QDs and H_2O_2. (c) Selectivity of N-Ti_3C_2 QDs toward H_2O_2 and metal ions (Na^+, K^+, Mg^{2+}, Ca^{2+}, Fe^{2+}, Zn^{2+}, Al^{3+}). (d) Selectivity of N-Ti_3C_2 QDs toward H_2O_2 and other reactive oxygen species ($^{\bullet}OH$, $O_2^{\bullet-}$, $^1O_2$). (e) XPS survey of N-Ti_3C_2 QDs after reacting with H_2O_2. (f) PLE spectra of N-Ti_3C_2 QDs before and after reacting with H_2O_2.

where E_{total} is total energy of the $Ti_3C_2T_x$ or N-$Ti_3C_2T_x$ system with the adsorbed $^{\bullet}OH$, $E_{surface}$ is total energy of the $Ti_3C_2T_x$ or N-$Ti_3C_2T_x$ system alone, and $E_{^{\bullet}OH,isolated}$ is the energy of an isolated $^{\bullet}OH$ (a single $^{\bullet}OH$ in a supercell), respectively. With such a scheme, negative adsorption energy means an exothermic process, while positive binding energy indicates an endothermic process. The initial height of $^{\bullet}OH$ is set to be 1 Å on the $Ti_3C_2T_x$ or N-$Ti_3C_2T_x$ surface. After full relaxation of these configurations, adsorption energies of $^{\bullet}OH$ for $Ti_3C_2T_x$ and N-$Ti_3C_2T_x$ systems are calculated using eq 1 and are shown in Figure 4a,b. The negative adsorption energies indicate that $^{\bullet}OH$ can be spontaneously adsorbed by the $Ti_3C_2T_x$ and N-$Ti_3C_2T_x$ systems. Notably, the adsorption energies of $^{\bullet}OH$ on the N-$Ti_3C_2T_x$ surface are lower than that on the corresponding $Ti_3C_2T_x$, especially for the −F (−0.58 eV for $Ti_3C_2T_x$ vs −2.16 eV for N-$Ti_3C_2T_x$) and −O (−0.19 eV for $Ti_3C_2T_x$ vs −1.97 eV for N-$Ti_3C_2T_x$)-terminated modes, suggesting that N-$Ti_3C_2T_x$ has much stronger adsorption capacity on $^{\bullet}OH$ than $Ti_3C_2T_x$.

Next, we explore the $^{\bullet}OH$ adsorption process and the corresponding charge-transfer procedure. Figure 4a shows the relaxed structures of $^{\bullet}OH$ adsorbed on the $Ti_3C_2T_x$ and N-$Ti_3C_2T_x$ surfaces. It could be seen that following the adsorption of $^{\bullet}OH$ onto the $Ti_3C_2O_2H_2$/N-$Ti_3C_2O_2H_2$ surface, the adsorbed $^{\bullet}OH$ combines with a proton to form hydration water. The distance between an O atom of the adsorbed $^{\bullet}OH$ and the N-$Ti_3C_2O_2H_2$ surface is 0.046 Å, which is shorter than the distance between the O atom and the $Ti_3C_2O_2H_2$ surface 0.048 Å. It implies that the bonding force for hydration water is enhanced by N atoms doping. Compared with $Ti_3C_2O_2$/$Ti_3C_2F_2$, the length of the Ti−O bond for −O and −F-terminated N-$Ti_3C_2O_2$/N-$Ti_3C_2F_2$ decreases by 0.007 and 0.002 Å, respectively. Thus, the decrease in the distance demonstrates that the N atom makes N-$Ti_3C_2T_x$ easier to absorb $^{\bullet}OH$.

To further study the underlying mechanism, the electronic structure is needed to be interpreted. The underlying density of states (DOS) of $Ti_3C_2T_x$ and N-$Ti_3C_2T_x$ are plotted in Figure 4c. For comparison of the DOS of $Ti_3C_2T_x$ and N-$Ti_3C_2T_x$, a pronounced new peak located at a low energy level is emerged after doping a N atom for N-$Ti_3C_2T_x$. It indicates that the free-electron concentration increases. From the DOS related to the Ti atom and the N atom of N-$Ti_3C_2T_x$, we find that the new peaks of N-$Ti_3C_2T_x$ are formed mostly by the Ti atom and the N atom. The Ti atom orbital hybridized with the N orbital at the site in the new peak, indicating that a chemical bond is formed between them. The enhanced reaction of the associated Ti atom leads to stronger adsorption capacity on $^{\bullet}OH$ for N-$Ti_3C_2T_x$ compared to $Ti_3C_2T_x$.

Figure 4d shows different charge densities. For a $Ti_3C_2O_2H_2$-OH/N-$Ti_3C_2O_2H_2$-OH system, there is obvious charge accumulation between a H atom and $^{\bullet}OH$, proving the bonding between them. There is also charge depletion of a Ti atom, demonstrating that Ti is losing electrons. In addition, for the $Ti_3C_2O_2$-OH/N-$Ti_3C_2O_2$-OH/$Ti_3C_2F_2$-OH/N-$Ti_3C_2F_2$-OH system, there is also charge accumulation between the Ti atom and the O atom of $^{\bullet}OH$, suggesting the bonding between them. It is also obvious that the Ti atom loses an electron and the accumulated charge is closer to the O atom of $^{\bullet}OH$. The redistribution of charge density gives rise to a variety of valences for the Ti atom, which corresponds to the XPS survey, as shown in Figure 3a,f.

H_2O_2 Sensing. As a typical kind of ROS, H_2O_2 is a significant oxidative stress indicator as well as a signaling molecule in biological systems. Due to the rapid and sensitive reactivity to H_2O_2, the prepared N-Ti_3C_2 QDs are used to monitor the trace amount of H_2O_2. The UV−vis spectrum of

https://doi.org/10.1021/acsami.1c11242
ACS Appl. Mater. Interfaces 2021, 13, 42442−42450

Table 1. Comparison of the H_2O_2 Detection Performance

method	system	limit of detection	linear range	time	references
electrochemical	Au-MnO	8 nM	20 nM−15.11 mM	tens of minutes	22
electrochemical	HRP/DMSNs	0.11 μM	0.5−103 μM	tens of minutes	38
chemiluminescence	BPNS/GCE	0.96 nM	1 nM−1 μM	few seconds	39
chemiluminescence	CF-$CoFe_2O_4$ NPs-luminol-H_2O_2-GOx	500 pM	1.0 nM−4.0 μM	tens of minutes	40
fluorescence	Eu-MOF	33.5 nM	0.05−2 μM	tens of minutes	23
fluorescence	SWNT/collagen		12.5−400 nM	few seconds	41
fluorescence	FRET		0.7−200 μM	few seconds	42
fluorescence	g-C_3N_4	50 nM	0.1−2000 μM	tens of minutes	43
fluorescence	TPE-HPro	100 nM	3−200 μM	tens of minutes	44
fluorescence	PVP-AuNPs	0.8 μM	1−100 μM	few seconds	45
fluorescence	N-Ti_3C_2 QDs	1.2 nM	5 nM−5.5 μM	15 s	this work

an N-Ti_3C_2 QD aqueous solution (Figure S9) exhibits two absorption peaks at 260 and 320 nm, respectively. Under 365 nm UV irradiation, N-Ti_3C_2 QDs emit a strong blue fluorescence with a corresponding emission position of 445 nm in the photoluminescence (PL) spectra. The fluorescence is steady under 360 nm light excitation in the pH range of 2.0−12.0 (Figure S10). Compared to Ti_3C_2 QDs, N-Ti_3C_2 QDs exhibit enhanced fluorescence performance, which could be ascribed to an increased carrier lifetime after N doping.[46] This outstanding fluorescence property makes N-Ti_3C_2 QDs to be served as fluorescent probes. As shown in Figure 5a, the H_2O_2 detection assay was carried out by adding different amounts of H_2O_2 to an N-Ti_3C_2 QD aqueous solution. With the increase in the H_2O_2 concentration, the PL intensity of solutions decreases accordingly (Figure 5a). Figure 5b shows great linearity from 5 to 100 nM of the H_2O_2 concentration with a high *R*-square value (0.9882). The fluorescence intensity of N-Ti_3C_2 QDs continues to decrease with the H_2O_2 concentration between 0.1 and 5.5 μM (inset of Figure 5b). The limit of detection based on $3\sigma/k$ (where σ is the standard deviation of the blank measurement and k is the slope of the calibration graph) is 1.2 nM, which is the lowest detection limit till now (Table 1).

To further verify the selectivity of an N-Ti_3C_2 QD probe to H_2O_2, the PL intensity in response to various ions, including Na^+, K^+, Mg^{2+}, Ca^{2+}, Fe^{2+}, Zn^{2+}, Al^{3+} ions, and ROS, are investigated. As shown in Figure 5c, N-Ti_3C_2 QDs exhibit a low response to metal ions because their fluorescence property is dominated by the intrinsic structure and surface states of N-Ti_3C_2 QDs. Furthermore, N-Ti_3C_2 QDs show a 5-fold higher fluorescence quenching ratio response to H_2O_2 over similar ROS, including $^{\bullet}OH$, $O_2^{\bullet-}$, and $^1O_2$, as shown in Figure 5d. This indicates that N-Ti_3C_2 QDs have excellent selectivity for detecting H_2O_2 and show promising potential to be applied in complex biological environments. XPS measurement was carried out after the reaction of N-Ti_3C_2 QDs with H_2O_2 (Figure 5e and Table S1). Compared with original N-Ti_3C_2 QDs (Figure 2c), the element ratio of F, N, and Ti in N-Ti_3C_2 QDs significantly reduced while the oxygen content increased, indicating that N-Ti_3C_2 QDs are oxidized to a certain extent after sensing for H_2O_2. This oxidation process could not only destroy the intrinsic structure of N-Ti_3C_2 QDs but also change the surface defect states and functional group composition. As shown in Figure 5f (PLE spectra), two electronic transitions of N-Ti_3C_2 QDs at 358 and 400 nm are regarded as intrinsic absorption and the trapping of the excited-state energy by the surface states, respectively.[46,47] The intrinsic absorption at 358 nm decreased by 14.8% and the functional groups' absorption at 400 nm decreased by 15.7% after reacting with H_2O_2. The decrease in the intrinsic absorption is attributed to the gradual oxidation of the MXene structure. The decrease in functional groups' absorption is owing to the oxidation of Ti, which breaks the surface Ti−OH and Ti−F bonds. The change in the intrinsic structure and surface defect states cause a gradual reduction in the PL intensity.

CONCLUSIONS

In this work, N-Ti_3C_2 QDs were successfully synthesized by a hydrothermal method using ammonium hydroxide as a nitrogen source. The as-prepared N-Ti_3C_2 QDs exhibit superior free-radical scavenging ability than Ti_3C_2 QDs. CV tests demonstrate that the doped N atoms promote the electronic transport between N-Ti_3C_2 QDs and free radicals, which is further confirmed by DFT simulations. DFT calculations show that N doping efficiently promotes the $^{\bullet}OH$ adsorption ability of −F and −O functional groups. $^{\bullet}OH$ is scavenged through the $^{\bullet}OH$ adsorption in the functional groups and further charge transfer from $^{\bullet}OH$ to a Ti element in N-Ti_3C_2 QDs. In addition, the DFT results indicate that −OH exhibits the highest $^{\bullet}OH$ adsorption activity among the functional groups in N-Ti_3C_2 QDs. Moreover, after the addition of H_2O_2, the fluorescence of N-Ti_3C_2 QDs gradually decreased. As a real-time fluorescent probe, the detection limit of the fluorescence response of an N-Ti_3C_2 QD sensor to H_2O_2 is as low as 1.2 nM. Our work facilitates the understanding of the antioxidant mechanism of MXene-based materials and provides a potential candidate for H_2O_2 sensing in the biology field.

EXPERIMENTAL SECTION

Preparation of N-Ti_3C_2 QDs. The Ti_3AlC_2 powder was purchased from the Laizhou Kai Kai Ceramic Materials Company Limited. First of all, the Ti_3AlC_2 (10 g) powder was dissolved in 100 mL of HF (50%) and etched at room temperature for 18 h. After centrifugation (3500 rpm), the sediment was washed five to six times with deionized water until the pH reached 6. The $Ti_3C_2T_x$ powder was obtained by drying at room temperature for 24 h. Then, the $Ti_3C_2T_x$ (0.3 g) powder was dissolved in deionized water (20 mL) by ultrasonication. The pH of the solution was adjusted to 9 with ammonia water and the solution was transferred into a 100 mL Teflon-lined stainless steel autoclave at 120 °C for 6 h to obtain N-Ti_3C_2 QDs. Ti_3C_2 QDs were prepared without ammonia water added by hydrothermal treatment at 150 °C. GQDs were prepared by the electrochemical method, as reported in our previous work.[48] GO was prepared by the modified Hummers method.[49]

Scavenging DPPH and Hydroxyl Radicals. As a stable radical, 2,2-diphenyl-1-picrylhydrazyl radical ($DPPH^{\bullet}$) is commonly used to

https://doi.org/10.1021/acsami.1c11242
ACS Appl. Mater. Interfaces 2021, 13, 42442−42450

test the antioxidant properties of antioxidants. It can combine with the hydrogen atoms of the antioxidant to form a stable H-DPPH complex along with the color change. The concentration of DPPH$^{\bullet}$ can be monitored by its characteristic absorption peak at 517 nm. A total of 1 mL of DPPH$^{\bullet}$ alcohol (100 μM) solutions was mixed with 1 mL of an N-Ti_3C_2 QD (100 μg/mL) aqueous solution and incubated 1 h in the dark. The residual DPPH$^{\bullet}$ was detected by its characteristic absorption peak (517 nm). TiO_2 can generate a hydroxyl radical in the UV light (365 nm) and *p*-phthalic acid (PTA) captures it to form fluorescent product 2-hydroxyterephthalic acid (excitation wavelength: 315 nm, emission peak: 430 nm). The activity of antioxidants to scavenge hydroxyl radicals was represented by detecting the intensity of the fluorescence after the reaction.

Dye Protect Assay. Overall, 2 mL of a solution containing PBS (25 mM), *p*-phthalic acid (0.5 mM), TiO_2 (50 μg/mL), and 50 μg/mL N-Ti_3C_2 QDs, Ti_3C_2 QDs, GO, or GQDs was irradiated by ultraviolet light (8 W, 365 nm) for 1 h. Then, the fluorescence intensity (430 nm) of 2-hydroxyterephthalic acid was detected by PL spectra. The control sample was conducted in the same condition except that no N-Ti_3C_2 QDs were added. Rhodamine B (RhB) was used as a model target molecule for an oxidant attack. Overall, 2 mL of the solution containing TiO_2 (P25, 50 μg/mL), RhB (10 μM), and antioxidants (250 μg/mL) was irradiated by the UV light (8 W, 365 nm) for 1 h. The concentration of the remaining RhB was monitored by its absorption spectra (552 nm).

H_2O_2-Sensing Assay. H_2O_2 was diluted with deionized water and (was) added to 2 mL of an N-Ti_3C_2 QD solution (50 μg/mL) according to a series of concentration gradients (0−5.5 μM), and then was slowly shaken and allowed to stand still for 15 s. The fluorescence spectra were obtained for the mixture solution under 360 nm excitation. In selective experiments, $^1O_2$ was generated from the online reaction of a NaClO solution with H_2O_2.[50] $^{\bullet}OH$ was produced by the Fenton reaction (Fe^{2+}−EDTA/H_2O_2 = 1:1).[51] $O_2^{\bullet-}$ was generated from a hypoxanthine/xanthine oxidase system.[52] Considering the reaction rate of different ROS and the fluctuation of PL intensity as time, the fluorescence intensity change of N-Ti_3C_2 QD solutions to H_2O_2, $^{\bullet}OH$, and $^1O_2$ sensing were recorded after 15 s of the reaction. As for $O_2^{\bullet-}$ sensing, the intensity change was recorded after 1800 s of the reaction. Metal ions (Na^+, K^+, Mg^{2+}, Ca^{2+}, Fe^{2+}, Zn^{2+}, and Al^{3+}) and free radicals with a concentration of 2 μM as an interference were determined.

DFT Calculations. All DFT calculations in this work are carried out using the Vienna Ab initio Simulation Program (VASP). The electron−ion interaction is described by the projector augmented wave (PAW) method;[53] the generalized gradient approximation (GGA) functional of Perdew, Burke, and Ernzerhof (PBE)[54] is used to describe the electron exchange−correlation. The energy cutoff for the planewave basis is set to 500 eV to ensure the convergence of the calculations. The Brillouin zone integration is performed within the Monkhorst−Pack scheme using a 3 × 3 × 1 mesh for the geometry optimizations.[55] Systematic calculations presented here have been performed in a 3 × 3 × 1 supercell with a periodic boundary condition. For an N-$Ti_3C_2T_x$ system, the composition is one C atom replaced by one N atom. To avoid interactions between neighboring slabs along the *z*-axis, a vacuum layer of 20 Å is included. Both the supercell size and atomic positions are relaxed to equilibrium, and energy minimization is continued until the forces on all atoms are converged to smaller than 10^{-3} eV/Å. The total energy of each system is relaxed until the difference value is smaller than 10^{-7} eV.

Characterization. Scanning electron microscopy (SEM) images were obtained using a JSM-7401 electron microscope. Transmission electron microscopy (TEM) was measured using a JEM-2010 electron microscope. Atomic force microscopy (AFM) images were performed with a Bruker Dimension Icon microscope in ambient air. The XRD patterns of the QDs were measured using a D/MAX 2500H X-ray diffractometer with Cu Kα radiation. Ultraviolet−visible spectroscopy was performed using a TU-1900 spectrophotometer and photoluminescence spectra of samples were obtained using a 4500 Fluorimeter. Fourier transform infrared spectra (FT-IR) were recorded using a NEXUS spectrometer 670. X-ray photoelectron spectroscopy (XPS) was recorded using an ESCALAB 250Xi electron spectrometer with an Al monochromatic Kα radiation ($h\nu$ = 1486.6 eV) source. XPS survey was conducted before and after N-Ti_3C_2 QDs reacted with H_2O_2. Raman spectra were carried out using an RM 2000 Microscopic Confocal Raman Spectrometer (Renishaw PLC, England) under a He−Ne laser with an excitation wavelength of 632.8 nm. The electrochemical cyclic voltammetry was tested at a CHI 660D working station with N-Ti_3C_2 QDs or Ti_3C_2 QDs modified glassy carbon electrode (GCE) as a working electrode, a Pt plate as a counter electrode, and Ag/AgCl as a reference electrode. The GCE electrode was burnished with alumina powder before the experiment, and then ultrasonicated 20 min in ethanol and deionized water, respectively. The electrolyte was KCl (0.1 M) containing potassium ferricyanide (0.5 mM $K_3[Fe(CN)_6]$) and potassium ferrocyanide (0.5 mM $K_4Fe(CN)_6{\cdot}3H_2O$). The data were recorded after about four cycles under steady-state conditions.

■ ASSOCIATED CONTENT

Supporting Information

The Supporting Information is available free of charge at https://pubs.acs.org/doi/10.1021/acsami.1c11242.

XRD patterns of Ti_3AlC_2 and $Ti_3C_2T_x$, TEM image, FT-IR spectrum, XPS survey of Ti_3C_2 QDs, DPPH$^{\bullet}$ scavenging efficiency of N-Ti_3C_2 QDs and Ti_3C_2 QDs, Raman spectra of N-Ti_3C_2 QDs before and after reacting with DPPH$^{\bullet}$. UV−vis spectrum of N-Ti_3C_2 QDs, and PL spectra (Ex = 380 nm) of Ti_3C_2 QDs and N-Ti_3C_2 QDs (PDF)

■ AUTHOR INFORMATION

Corresponding Authors

Yan Li − *School of Materials Science and Engineering, University of Science and Technology Beijing, Beijing 100083, P. R. China;* orcid.org/0000-0001-5017-4592; Email: liyan2011@ustb.edu.cn

Liangti Qu − *Key Laboratory for Advanced Materials Processing Technology, Ministry of Education of China, State Key Laboratory of Tribology, Department of Mechanical Engineering and Key Lab of Organic Optoelectronics and Molecular Engineering of Ministry of Education, Department of Chemistry, Tsinghua University, Beijing 100084, P. R. China;* orcid.org/0000-0002-0161-3816; Email: lqu@mail.tsinghua.edu.cn

Authors

Lifeng Wang − *School of Materials Science and Engineering, University of Science and Technology Beijing, Beijing 100083, P. R. China; State Key Laboratory of Tribology, Department of Mechanical Engineering, Tsinghua University, Beijing 100084, P. R. China*

Ningning Zhang − *LCP, Institute of Applied Physics and Computational Mathematics, Beijing 100088, P. R. China*

Wenhui Kong − *School of Materials Science and Engineering, University of Science and Technology Beijing, Beijing 100083, P. R. China*

Jingyun Gou − *School of Materials Science and Engineering, University of Science and Technology Beijing, Beijing 100083, P. R. China*

Yujuan Zhang − *School of Materials Science and Engineering, University of Science and Technology Beijing, Beijing 100083, P. R. China*

Lu-Ning Wang − *School of Materials Science and Engineering, University of Science and Technology Beijing, Beijing 100083, P. R. China*

Guanghua Yu − *School of Materials Science and Engineering, University of Science and Technology Beijing, Beijing 100083, P. R. China*

Ping Zhang − *LCP, Institute of Applied Physics and Computational Mathematics, Beijing 100088, P. R. China*

Huhu Cheng − *Key Laboratory for Advanced Materials Processing Technology, Ministry of Education of China, State Key Laboratory of Tribology, Department of Mechanical Engineering and Key Lab of Organic Optoelectronics and Molecular Engineering of Ministry of Education, Department of Chemistry, Tsinghua University, Beijing 100084, P. R. China;* orcid.org/0000-0002-7626-1368

Complete contact information is available at: https://pubs.acs.org/10.1021/acsami.1c11242

Author Contributions

[⊥]L.W. and N.Z. contributed equally to this work.

Notes

The authors declare no competing financial interest.

■ ACKNOWLEDGMENTS

This work was supported by the National Natural Science Foundation of China (Grant No. 21674011), the Beijing Municipal Natural Science Foundation (Grant No. 2172040), and the Fundamental Research Funds for the Central Universities (Grant No. FRF-MP-20-23Z).

■ REFERENCES

(1) Yang, B. W.; Chen, Y.; Shi, J. L. Reactive Oxygen Species (ROS)-Based Nanomedicine. *Chem. Rev.* **2019**, *119*, 4881−4985.

(2) Radi, R. Oxygen Radicals, Nitric Oxide, and Peroxynitrite: Redox Pathways in Molecular Medicine. *Proc. Natl. Acad. Sci. U.S.A.* **2018**, *115*, 5839−5848.

(3) Weidinger, A.; Kozlov, A. V. Biological Activities of Reactive Oxygen and Nitrogen Species: Oxidative Stress versus Signal Transduction. *Biomolecules* **2015**, *5*, 472−484.

(4) Sies, H.; Jones, D. P. Reactive Oxygen Species (ROS) as Pleiotropic Physiological Signalling Agents. *Nat. Rev. Mol. Cell Biol.* **2020**, *21*, 363−383.

(5) Perera, R. M.; Bardeesy, N. CANCER when Antioxidants are Bad. *Nature* **2011**, *475*, 43−44.

(6) Lin, M. T.; Beal, M. F. Mitochondrial Dysfunction and Oxidative Stress in Neurodegenerative Diseases. *Nature* **2006**, *443*, 787−795.

(7) Hansson, G. K.; Libby, P. The Immune Response in Atherosclerosis: A Double-Edged Sword. *Nat. Rev. Immunol.* **2006**, *6*, 508−519.

(8) Ni, D.; Jiang, D.; Kutyreff, C. J.; Lai, J.; Yan, Y.; Barnhart, T. E.; Yu, B.; Im, H. J.; Kang, L.; Cho, S. Y.; Liu, Z.; Huang, P.; Engle, J. W.; Cai, W. Molybdenum-Based Nanoclusters act as Antioxidants and Ameliorate Acute Kidney Injury in Mice. *Nat. Commun.* **2018**, *9*, No. 5421.

(9) Soh, M.; Kang, D.-W.; Jeong, H.-G.; Kim, D.; Kim, D. Y.; Yang, W.; Song, C.; Baik, S.; Choi, I.-Y.; Ki, S.-K.; Kwon, H. J.; Kim, T.; Kim, C. K.; Lee, S.-H.; Hyeon, T. Ceria-Zirconia Nanoparticles as an Enhanced Multi-Antioxidant for Sepsis Treatment. *Angew. Chem., Int. Ed.* **2017**, *56*, 11399−11403.

(10) Kim, C. K.; Kim, T.; Choi, I.-Y.; Soh, M.; Kim, D.; Kim, Y.-J.; Jang, H.; Yang, H.-S.; Kim, J. Y.; Park, H.-K.; Park, S. P.; Park, S.; Yu, T.; Yoon, B.-W.; Lee, S.-H.; Hyeon, T. Ceria Nanoparticles that can Protect against Ischemic Stroke. *Angew. Chem., Int. Ed.* **2012**, *51*, 11039−11043.

(11) Qiu, Y.; Wang, Z.; Owens, A. C.; Kulaots, I.; Chen, Y.; Kane, A. B.; Hurt, R. H. Antioxidant Chemistry of Graphene-Based Materials and Its Role in Oxidation Protection Technology. *Nanoscale* **2014**, *6*, 11744−11755.

(12) Chen, W.; Ouyang, J.; Yi, X.; Xu, Y.; Niu, C.; Zhang, W.; Wang, L.; Sheng, J.; Deng, L.; Liu, Y. N.; Guo, S. Black Phosphorus Nanosheets as a Neuroprotective Nanomedicine for Neurodegenerative Disorder Therapy. *Adv. Mater.* **2018**, *30*, No. 1703458.

(13) Chen, T.; Zou, H.; Wu, X.; Liu, C.; Situ, B.; Zheng, L.; Yang, G. Nanozymatic Antioxidant System Based on MoS_2 Nanosheets. *ACS Appl. Mater. Interfaces* **2018**, *10*, 12453−12462.

(14) Ren, X. Y.; Huo, M. F.; Wang, M. M.; Lin, H.; Zhang, X. X.; Yin, J.; Chen, Y.; Chen, H. H. Highly Catalytic Niobium Carbide (MXene) Promotes Hematopoietic Recovery after Radiation by Free Radical Scavenging. *ACS Nano* **2019**, *13*, 6438−6454.

(15) Wang, L.; Li, Y.; Zhao, L.; Qi, Z.; Gou, J.; Zhang, S.; Zhang, J. Z. Recent Advances in Ultrathin Two-Dimensional Materials and Biomedical Applications for Reactive Oxygen Species Generation and Scavenging. *Nanoscale* **2020**, *12*, 19516−19535.

(16) Wang, L. F.; Li, Y.; Wang, Y. M.; Kong, W. H.; Lu, Q. P.; Liu, X. G.; Zhang, D. W.; Qu, L. T. Chlorine-Doped Graphene Quantum Dots with Enhanced Anti- and Pro-Oxidant Properties. *ACS Appl. Mater. Interfaces* **2019**, *11*, 21822−21829.

(17) Zhao, S. J.; Lan, M. H.; Zhu, X. Y.; Xue, H. T.; Ng, T. W.; Meng, X. M.; Lee, C. S.; Wang, P. F.; Zhang, W. J. Green Synthesis of Bifunctional Fluorescent Carbon Dots from Garlic for Cellular Imaging and Free Radical Scavenging. *ACS Appl. Mater. Interfaces* **2015**, *7*, 17054−17060.

(18) Xue, Q.; Zhang, H. J.; Zhu, M. S.; Pei, Z. X.; Li, H. F.; Wang, Z. F.; Huang, Y.; Huang, Y.; Deng, Q. H.; Zhou, J.; Du, S. Y.; Huang, Q.; Zhi, C. Y. Photoluminescent Ti_3C_2 MXene Quantum Dots for Multicolor Cellular Imaging. *Adv. Mater.* **2017**, *29*, No. 1604847.

(19) Lu, S.; Sui, L.; Liu, Y.; Yong, X.; Xiao, G.; Yuan, K.; Liu, Z.; Liu, B.; Zou, B.; Yang, B. White Photoluminescent Ti_3C_2 MXene Quantum Dots with Two-Photon Fluorescence. *Adv. Sci.* **2019**, *6*, No. 1801470.

(20) Zhao, L.; Wang, Z.; Li, Y.; Wang, S.; Wang, L.; Qi, Z.; Ge, Q.; Liu, X.; Zhang, J. Z. Designed Synthesis of Chlorine and Nitrogen Co-Doped Ti_3C_2 MXene Quantum Dots and Their Outstanding Hydroxyl Radical Scavenging Properties. *J. Mater. Sci. Technol.* **2021**, *78*, 30−37.

(21) Sobotta, M. C.; Liou, W.; Stocker, S.; Talwar, D.; Oehler, M.; Ruppert, T.; Scharf, A. N.; Dick, T. P. Peroxiredoxin-2 and STAT3 Form a Redox Relay for H_2O_2 Signaling. *Nat. Chem. Biol.* **2015**, *11*, 64−70.

(22) Zhu, H. Y.; Sigdel, A.; Zhang, S.; Su, D.; Xi, Z.; Li, Q.; Sun, S. H. Core/Shell Au/MnO Nanoparticles Prepared Through Controlled Oxidation of AuMn as an Electrocatalyst for Sensitive H_2O_2 Detection. *Angew. Chem., Int. Ed.* **2014**, *53*, 12508−12512.

(23) Cui, Y.; Chen, F.; Yin, X. B. A Ratiometric Fluorescence Platform Based on Boric-Acid-Functional Eu-MOF for Sensitive Detection of H_2O_2 and Glucose. *Biosens. Bioelectron.* **2019**, *135*, 208−215.

(24) Liu, Q. Y.; Yang, Y. T.; Li, H.; Zhu, R. R.; Shao, Q.; Yang, S. G.; Xu, J. J. NiO Nanoparticles Modified with 5,10,15,20-tetrakis(4-carboxyl pheyl)-porphyrin: Promising Peroxidase Mimetics for H_2O_2 and Glucose Detection. *Biosens. Bioelectron.* **2015**, *64*, 147−153.

(25) Ma, B.; Kong, C. C.; Hu, X. X.; Liu, K.; Huang, Q.; Lv, J.; Lu, W. J.; Zhang, X. J.; Yang, Z. M.; Yang, S. A Sensitive Electrochemical Nonenzymatic Biosensor for the Detection of H_2O_2 Released from Living Cells Based on Ultrathin Concave Ag Nanosheets. *Biosens. Bioelectron.* **2018**, *106*, 29−36.

(26) Lv, J.; Kong, C. C.; Liu, K.; Yin, L.; Ma, B.; Zhang, X. J.; Yang, S.; Yang, Z. M. Surfactant-Free Synthesis of Cu_2O Yolk-Shell Cubes Decorated with Pt Nanoparticles for Enhanced H_2O_2 Detection. *Chem. Commun.* **2018**, *54*, 8458−8461.

(27) Mohammadniaei, M.; Yoon, J.; Lee, T.; Bharate, B. G.; Jo, J.; Lee, D.; Choi, J. W. Electrochemical Biosensor Composed of Silver Ion-Mediated dsDNA on Au-Encapsulated Bi_2Se_3 Nanoparticles for the Detection of H_2O_2 Released from Breast Cancer Cells. *Small* **2018**, *14*, No. 1703970.

(28) Ren, H.; Long, Z.; Cui, M. C.; Shao, K.; Zhou, K. X.; Ouyang, J.; Na, N. Dual-Functional Nanoparticles for In Situ Sequential

Detection and Imaging of ATP and H_2O_2. *Small* **2016**, *12*, 3920−3924.
(29) Li, Z.; Yu, L.; Milligan, C.; Ma, T.; Zhou, L.; Cui, Y.; Qi, Z.; Libretto, N.; Xu, B.; Luo, J.; Shi, E.; Wu, Z.; Xin, H.; Delgass, W. N.; Miller, J. T.; Wu, Y. Two-Dimensional Transition Metal Carbides as Supports for Tuning the Chemistry of Catalytic Nanoparticles. *Nat. Commun.* **2018**, *9*, No. 5258.
(30) Lukatskaya, M. R.; Mashtalir, O.; Ren, C. E.; Dall'Agnese, Y.; Rozier, P.; Taberna, P. L.; Naguib, M.; Simon, P.; Barsoum, M. W.; Gogotsi, Y. Cation Intercalation and High Volumetric Capacitance of Two-Dimensional Titanium Carbide. *Science* **2013**, *341*, 1502−1505.
(31) Ghidiu, M.; Lukatskaya, M. R.; Zhao, M. Q.; Gogotsi, Y.; Barsoum, M. W. Conductive Two-Dimensional Titanium Carbide 'Clay' with High Volumetric Capacitance. *Nature* **2014**, *516*, 78−81.
(32) Guo, Z.; Zhu, X. H.; Wang, S. G.; Lei, C. Y.; Huang, Y.; Nie, Z.; Yao, S. Z. Fluorescent Ti_3C_2 MXene Quantum Dots for an Alkaline Phosphatase Assay and Embryonic Stem Cell Identification Based on the Inner Filter Effect. *Nanoscale* **2018**, *10*, 19579−19585.
(33) Ruiz, V.; Yate, L.; Garcia, I.; Cabanero, G.; Grande, H. J. Tuning the Antioxidant Activity of Graphene Quantum Dots: Protective Nanomaterials against Dye Decoloration. *Carbon* **2017**, *116*, 366−374.
(34) Liu, Y.; Ai, K.; Ji, X.; Askhatova, D.; Du, R.; Lu, L.; Shi, J. Comprehensive Insights into the Multi-Antioxidative Mechanisms of Melanin Nanoparticles and Their Application To Protect Brain from Injury in Ischemic Stroke. *J. Am. Chem. Soc.* **2017**, *139*, 856−862.
(35) Zhang, L.; Diao, S.; Nie, Y.; Yan, K.; Liu, N.; Dai, B.; Xie, Q.; Reina, A.; Kong, J.; Liu, Z. Photocatalytic Patterning and Modification of Graphene. *J. Am. Chem. Soc.* **2011**, *133*, 2706−2713.
(36) Krishnamoorthy, K.; Veerapandian, M.; Yun, K.; Kim, S. J. The Chemical and Structural Analysis of Graphene Oxide with Different Degrees of Oxidation. *Carbon* **2013**, *53*, 38−49.
(37) Yu, X.; Zhang, M.; Chen, J.; Li, Y.; Shi, G. Nitrogen and Sulfur Codoped Graphite Foam as a Self-Supported Metal-Free Electrocatalytic Electrode for Water Oxidation. *Adv. Energy Mater.* **2016**, *6*, No. 1501492.
(38) Bai, G. M.; Xu, X.; Dai, Q. M.; Zheng, Q. Q.; Yao, Y. W.; Liu, S. Q.; Yao, C. An Electrochemical Enzymatic Nanoreactor Based on Dendritic Mesoporous Silica Nanoparticles for Living Cell H_2O_2 Detection. *Analyst* **2019**, *144*, 481−487.
(39) Ding, H. C.; Tang, Z. R.; Zhang, L.; Dong, Y. P. Electrogenerated Chemiluminescence of Black Phosphorus Nanosheets and Its Application in the Detection of H_2O_2. *Analyst* **2019**, *144*, 1326−1333.
(40) Fan, Y.; Huang, Y. The Effective Peroxidase-Like Activity of Chitosan-Functionalized $CoFe_2O_4$ Nanoparticles for Chemiluminescence Sensing of Hydrogen Peroxide and Glucose. *Analyst* **2012**, *137*, 1225−1231.
(41) Kim, J. H.; Patra, C. R.; Arkalgud, J. R.; Boghossian, A. A.; Zhang, J. Q.; Han, J. H.; Reuel, N. F.; Ahn, J. H.; Mukhopadhyay, D.; Strano, M. S. Single-Molecule Detection of H_2O_2 Mediating Angiogenic Redox Signaling on Fluorescent Single-Walled Carbon Nanotube Array. *ACS Nano* **2011**, *5*, 7848−7857.
(42) Qiao, J.; Liu, Z.; Tian, Y.; Wu, M.; Niu, Z. W. Multifunctional Self-Assembled Polymeric Nanoprobes for FRET-Based Ratiometric Detection of Mitochondrial H_2O_2 in Living Cells. *Chem. Commun.* **2015**, *51*, 3641−3644.
(43) Liu, J. W.; Luo, Y.; Wang, Y. M.; Duan, L. Y.; Jiang, J. H.; Yu, R. Q. Graphitic Carbon Nitride Nanosheets-Based Ratiometric Fluorescent Probe for Highly Sensitive Detection of H_2O_2 and Glucose. *ACS Appl. Mater. Interfaces* **2016**, *8*, 33439−33445.
(44) Song, Z.; Kwok, R. T.; Ding, D.; Nie, H.; Lam, J. W.; Liu, B.; Tang, B. Z. An AIE-Active Fluorescence Turn-On Bioprobe Mediated by Hydrogen-Bonding Interaction for Highly Sensitive Detection of Hydrogen Peroxide and Glucose. *Chem. Commun.* **2016**, *52*, 10076−10079.
(45) Chang, H. C.; Ho, J. A. A. Gold Nanocluster-Assisted Fluorescent Detection for Hydrogen Peroxide and Cholesterol Based on the Inner Filter Effect of Gold Nanoparticles. *Anal. Chem.* **2015**, *87*, 10362−10367.
(46) Xu, Q.; Ding, L.; Wen, Y. Y.; Yang, W. J.; Zhou, H. J.; Chen, X. Z.; Street, J.; Zhou, A. G.; Ong, W. J.; Li, N. High Photoluminescence Quantum Yield of 18.7% by using Nitrogen-Doped Ti_3C_2 MXene Quantum Dots. *J. Mater. Chem. C* **2018**, *6*, 6360−6369.
(47) Lashgari, H.; Abolhassani, M. R.; Boochani, A.; Elahi, S. M.; Khodadadi, J. Electronic and Optical Properties of 2D Graphene-Like Compounds Titanium Carbides and Nitrides: DFT Calculations. *Solid State Commun.* **2014**, *195*, 61−69.
(48) Wang, Y.; Kong, W.; Wang, L.; Zhang, J. Z.; Li, Y.; Liu, X.; Li, Y. Optimizing Oxygen Functional Groups in Graphene Quantum Dots for Improved Antioxidant Mechanism. *Phys. Chem. Chem. Phys.* **2019**, *21*, 1336−1343.
(49) Zhang, P.; Liu, F.; Liao, Q.; Yao, H.; Geng, H.; Cheng, H.; Li, C.; Qu, L. A Microstructured Graphene/Poly(N-isopropylacrylamide) Membrane for Intelligent Solar Water Evaporation. *Angew. Chem., Int. Ed.* **2018**, *57*, 16343−16347.
(50) Li, X. H.; Zhang, G. X.; Ma, H. M.; Zhang, D. Q.; Li, J.; Zhu, D. B. 4,5-Dimethylthio-4′-[2-(9-anthryloxy)ethylthio]tetrathiafulvalene, a highly selective and sensitive chemiluminescence probe for singlet oxygen. *J. Am. Chem. Soc.* **2004**, *126*, 11543−11548.
(51) Li, H. Y.; Shi, W.; Li, X. H.; Hu, Y. M.; Fang, Y.; Ma, H. M. Ferroptosis Accompanied by •OH Generation and Cytoplasmic Viscosity Increase Revealed via Dual-Functional Fluorescence Probe. *J. Am. Chem. Soc.* **2019**, *141*, 18301−18307.
(52) Wu, S. J.; Ma, C.; Gao, Y.; Su, Y.; Xia, Q.; Chen, Z. X.; Zhu, J. J. Dynamic Detection of Endogenous Hydroxyl Radicals at Single-Cell Level with Individual Ag-Au Nanocages. *Anal. Chem.* **2020**, *92*, 9940−9947.
(53) Kresse, G.; Joubert, D. From Ultrasoft Pseudopotentials to the Projector Augmented-Wave Method. *Phys. Rev. B* **1999**, *59*, 1758−1775.
(54) Kresse, G.; Furthmuller, J. Efficient Iterative Schemes for AB Initio Total-Energy Calculations using a Plane-Wave Basis Set. *Phys. Rev. B* **1996**, *54*, 11169−11186.
(55) Monkhorst, H. J.; Pack, J. D. Special Points for Brillouin-Zone Integrations. *Phys. Rev. B* **1976**, *13*, 5188−5192.

https://doi.org/10.1021/acsami.1c11242
ACS Appl. Mater. Interfaces 2021, 13, 42442−42450